Chen, Guangze; Zilberberg, Oded; Chen, Wei

Detection of Fermi arcs in Weyl semimetals through surface negative refraction

Published in:
Physical Review B

DOI:
10.1103/PhysRevB.101.125407

Published: 15/03/2020

Document Version
Publisher's PDF, also known as Version of record

Please cite the original version:
Chen, G., Zilberberg, O., & Chen, W. (2020). Detection of Fermi arcs in Weyl semimetals through surface negative refraction. *Physical Review B*, *101*(12), 1-9. Article 125407.
https://doi.org/10.1103/PhysRevB.101.125407

Detection of Fermi arcs in Weyl semimetals through surface negative refraction

Guangze Chen [1,2] Oded Zilberberg [1] and Wei Chen [1,3,4,*]

[1]*Institute for Theoretical Physics, ETH Zurich, 8093 Zurich, Switzerland*

[2]*Department of Applied Physics, Aalto University, 02150 Espoo, Finland*

[3]*National Laboratory of Solid State Microstructures and School of Physics, Nanjing University, Nanjing 210093, China*

[4]*College of Science, Nanjing University of Aeronautics and Astronautics, Nanjing 210016, China*

(Received 13 November 2019; accepted 20 February 2020; published 9 March 2020)

One of the main features of Weyl semimetals is the existence of Fermi arc surface states at their surface, which cannot be realized in pure two-dimensional systems in the absence of many-body interactions. Due to the gapless bulk of the semimetal, it is, however, challenging to observe clear signatures from the Fermi arc surface states. Here, we propose to detect such novel surface states via perfect negative refraction that occurs between two adjacent open surfaces with properly orientated Fermi arcs. Specifically, this phenomenon visibly manifests in nonlocal transport measurement, where the negative refraction generates a return peak in the real-space conductance. This provides a unique signature of the Fermi arc surface states. We discuss the appearance of this peak in both inversion- and time-reversal-symmetric Weyl semimetals, where the latter exhibits conductance oscillations due to multiple negative refraction scattering events.

DOI: 10.1103/PhysRevB.101.125407

I. INTRODUCTION

In recent years, the classification of topological phases of matter has been extended from topological insulators [1,2] to topological semimetals [3,4]. The latter involves gapless band structures with nontrivial topological properties. Depending on whether the gap closing occurs at isolated points in the Brillouin zone or along closed loops, they are mainly divided into Weyl/Dirac semimetals [5–10] and nodal-line semimetals [11]. The unique topological properties of these gapless band structures have been extensively explored using a wide variety of platforms, including solid-state materials [5–10,12–25], and also using photonic [26,27], phononic [28,29], and electric-circuit [30–32] metamaterials.

In Weyl semimetals, the gap closes at so-called Weyl points that are topologically robust against local perturbations in reciprocal space [33], which is beneficial for their experimental detection [12–23]. The band topology of Weyl semimetals is encoded in the monopole charge or Chern number of the Berry curvature field carried by each Weyl point. According to the topological bulk-boundary correspondence of Weyl semimetals, disconnected Fermi arcs appear in the surface Brillouin zone and span between the Weyl points [5,34]. Such exotic Fermi arcs serve as the fingerprint of Weyl semimetals, and their experimental identification has attracted great research interest [12–22].

Recent progress has been made on the observation of Fermi arc states in Weyl and Dirac semimetals by using angle-resolved photoemission spectroscopy [12–22] and quantum transport measurement [35,36]. In these experiments, both bulk and surface states appear in the measured observables, making it difficult to explicitly identify the Fermi arcs. Several phenomenon dominated by Fermi arc surfaces states have been predicted [37–39] but have yet to be observed. Therefore, there is a need to explore novel and unique transport properties that can facilitate the identification of Fermi arcs. Moreover, such particular transport signatures open an avenue for their control and manipulation for potential applications [40].

Fermi arcs indicate strong anisotropy that breaks rotational symmetry, in contrast to closed Fermi surfaces in normal metals. As a result, part of the scattering channels at the Fermi energy level is absent, serving as a source for unique transport properties, including negative refraction between different surfaces [41]. In reality, the electronic transport signatures will depend on the material details and their specific termination, both of which affect the Fermi arcs' orientation, dispersion, and length [12–17,42–44]. Notably, however, state-of-the-art fabrication techniques allow for controlled surface shaping on the level of a single layer [16,18,45,46], making it possible to explore the broad breadth of surface transport phenomena.

In Ref. [40], it was shown that perfect negative refraction occurs between two adjacent open surfaces when the respective Fermi arcs are properly orientated. In this work, we show that this scenario manifests for both $\mathcal{P}$- and $\mathcal{T}$-symmetric Weyl semimetals, which generates distinct spatial trajectories for electron propagation. In particular, we propose to detect the negative refraction via nonlocal scanning tunneling spectroscopy. The negative refraction manifests as a clear spatially resolved peak in the nonlocal conductance. Adverse effects, such as surface disorder and dispersive corrections to the Fermi arcs, do not qualitatively change this transport peak. Our results offer a decisive signature for the detection of the Fermi arcs and present Weyl semimetal surface transport as a platform to observe electronic negative refraction [47–50]. Experimental realization of our proposal is within reach as the surface Fermi arc orientation can be readily

*Corresponding author: pchenweis@gmail.com

controlled by the proper choice of the material termination [16,18,45,46].

This paper is organized as follows: in Sec. II, we show that arbitrary orientations of Fermi arcs can be described by a rotation transformation of an effective Hamiltonian. Based on the resulting effective surface Hamiltonian and using a tunneling approach, we calculate the nonlocal conductance between two local terminals in both inversion- ($\mathcal{P}$) and time-reversal- ($\mathcal{T}$) symmetric Weyl semimetals in Secs. III and IV, respectively. This serves as a direct signature of negative refraction. Finally, we discuss the experimental realization of our proposal and draw conclusions in Sec. V.

II. ORIENTED FERMI ARCS

In Weyl semimetals, Fermi arcs appear in the surface Brillouin zone, connecting the projection of two bulk Weyl points with opposite monopole charges. Within the surface Brillouin zone, the orientation of the Fermi arcs depends on the alignment of the bulk Weyl points relative to the termination direction of the sample. Therefore, by proper cutting of the sample, different orientations of the Fermi arcs can be obtained. To describe this orientation dependence, it is convenient to rotate the effective bulk Hamiltonian of the Weyl semimetal relative to fixed termination directions [51].

More concretely, we first consider the following minimal model of a $\mathcal{P}$-symmetric Weyl semimetal:

$$H(\boldsymbol{k}) = \hbar v(k_x\sigma_x + k_y\sigma_y) + M\left(k_0^2 - \boldsymbol{k}^2\right)\sigma_z, \tag{1}$$

where v, k_0, and $M > 0$ are parameters, $\boldsymbol{k} = (k_x, k_y, k_z)$ is the wave vector, and $\sigma_{x,y,z}$ are Pauli matrices acting on the two-band pseudospin space. By diagonalizing the Hamiltonian, one can find two Weyl points located at $\pm\boldsymbol{k}_0 = (0, 0, \pm k_0)$. We calculate the topologically protected surface states at an open surface in the $-y$ direction (surface I in Fig. 1). They are confined by $k_x^2 + k_z^2 < k_0^2$ and are described by the effective Hamiltonian (see Appendix A)

$$H_{\mathrm{I}}^0(k_x, k_z) = \hbar v k_x. \tag{2}$$

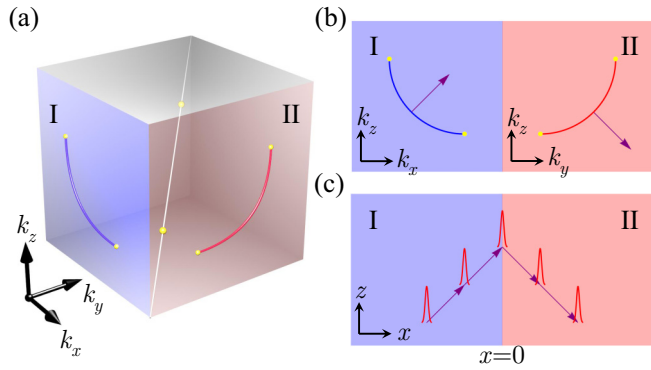

FIG. 1. Negative refraction between Fermi arcs at different surfaces of Weyl semimetals. (a) Sketch of a Weyl semimetal with oriented Fermi arcs (red and blue curves). (b) The red and blue surfaces form a junction that can be represented as a 2D scattering problem. The Fermi velocities (purple arrows) have opposite components parallel to the scattering line. (c) Perfect negative refraction of a surface wave packet due to the tilting of the Fermi arcs.

Similarly, the surface states on the open surface in the x direction (surface II in Fig. 1) are described by

$$H_{\mathrm{II}}^0(k_y, k_z) = \hbar v k_y. \tag{3}$$

On both surfaces, the states are parallel to the z direction. Therefore, Fermi arc states at a chemical potential within the bulk gap (henceforth taken at $E = 0$) are also parallel to the z direction. Correspondingly, due to the chirality of the surface states, electrons are fully transmitted without backscattering at a junction between surfaces I and II [see Fig. 1(b)].

Next, we perform a rotational transformation to the effective bulk Hamiltonian (1). In this way, we retain the same open boundary conditions and describe generally orientated Fermi arcs. A rotation about the axis $k_x = k_y$, $k_z = 0$ by an angle φ is defined by $H'(\boldsymbol{k}) = H(U^{-1}\boldsymbol{k})$ with the rotation operator

$$U(\varphi) = \begin{pmatrix} \cos^2\frac{\varphi}{2} & \sin^2\frac{\varphi}{2} & -\frac{\sin\varphi}{\sqrt{2}} \\ \sin^2\frac{\varphi}{2} & \cos^2\frac{\varphi}{2} & \frac{\sin\varphi}{\sqrt{2}} \\ \frac{\sin\varphi}{\sqrt{2}} & -\frac{\sin\varphi}{\sqrt{2}} & \cos\varphi \end{pmatrix}. \tag{4}$$

As a result, the bulk Weyl points are located at $U\boldsymbol{k}_0 = \pm k_0(-\frac{\sin\varphi}{\sqrt{2}}, \frac{\sin\varphi}{\sqrt{2}}, \cos\varphi)$, and the states on surface I can be described by the effective Hamiltonian

$$H_{\mathrm{I}}(k_x, k_z) = \hbar v'(\cos\theta k_x + \sin\theta k_z), \tag{5}$$

where v' is the renormalized velocity and $\theta = \tan^{-1}(\tan\varphi/\sqrt{2})$. The Fermi arc defined by $H_{\mathrm{I}} = 0$ is

$$\cos\theta k_x + \sin\theta k_z = 0 \tag{6}$$

and stretches between $\pm k_0(-\frac{\sin\varphi}{\sqrt{2}}, \cos\varphi)$. Note that our approach of rotating the effective bulk model and calculating the resulting surface dispersion is verified using microscopic lattice model simulations (see Appendix B). Similarly, on surface II

$$H_{\mathrm{II}}(k_y, k_z) = \hbar v'(\cos\theta k_y - \sin\theta k_z), \tag{7}$$

and the Fermi arc is defined by

$$\cos\theta k_y - \sin\theta k_z = 0 \tag{8}$$

and stretches between $\pm k_0(\frac{\sin\varphi}{\sqrt{2}}, \cos\varphi)$. Note that the two Fermi arcs have different orientations (see Fig. 1). For a finite θ, electrons incident on surface I can transfer only through the interface due to the lack of backscattering channels. At the same time, because the Fermi arcs on the two surfaces tilt in opposite directions, the velocity in the z direction is inverted, leading to negative refraction, as shown in Figs. 1(b) and 1(c).

In the following, we introduce a general dispersion term to the surface Hamiltonian

$$\begin{aligned} H_{\mathrm{I}}'(k_x, k_z) &= H_{\mathrm{I}} + \varepsilon_x, \\ H_{\mathrm{II}}'(k_y, k_z) &= H_{\mathrm{II}} - \varepsilon_y, \end{aligned} \tag{9}$$

with a parabolic dispersion $\varepsilon_{x,y} = d[k_0^2(1 - \sin^2\varphi/2) - k_{x,y}^2 - k_z^2]$. By tuning the dispersion strength d, the Fermi arcs become curved [see Figs. 1 and 2(b)]. Such curving captures the situation in real materials [12–23]. Moreover, the velocities of the surface states are also modified. In our following calculation, we assume that the dispersion does not invert the velocity in the x (y) direction on surface I (II). Note that the description of generally orientated Fermi arcs

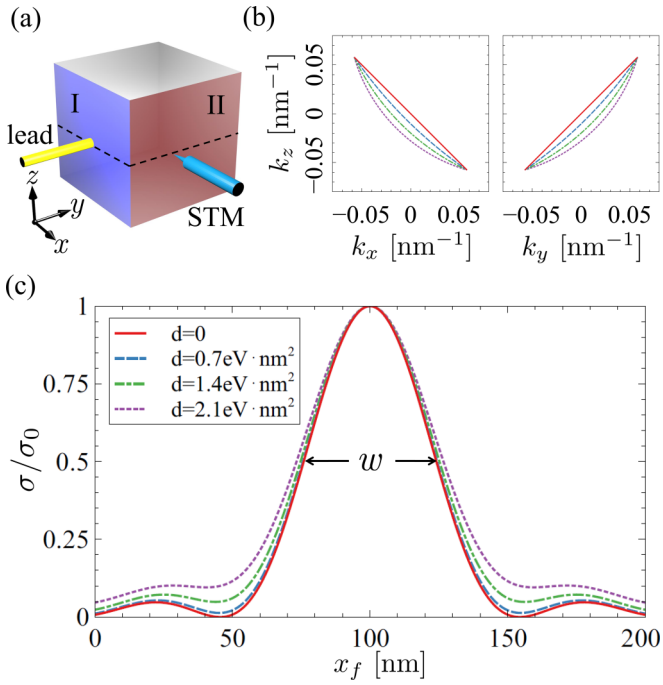

FIG. 2. Nonlocal conductance between surfaces of Weyl semimetals. (a) Sketch of the two-terminal setup for nonlocal conductance measurement. (b) Fermi arcs with different curvature controlled by d [see Eq. (9)], labeled by the legend in (c). (c) Nonlocal conductance $\sigma(\varepsilon = 0)$ for Fermi arcs with different curvature [see Eq. (11)], with parameters $\theta = \frac{\pi}{4}$, $k_0 = 0.1\,\mathrm{nm}^{-1}$, $v' = 10^6$ m/s, and $x_i = 100$ nm. The peak structure indicates the existence of negative refraction. The peak width w is comparable to π/k_0.

by rotation of the effective model works for both $\mathcal{P}$- and $\mathcal{T}$-symmetric Weyl semimetals. This approach is verified by numerical simulations of corresponding lattice models (see Appendix B).

III. NEGATIVE REFRACTION IN $\mathcal{P}$-SYMMETRIC WEYL SEMIMETALS

Next, we investigate nonlocal electron transport through the surface states [see the corresponding two-terminal setup in Fig. 2(a)]. For convenience, we unfold the two open surfaces to the x-z plane with the boundary located at $x = 0$ [Fig. 1(c)], which can be achieved by the replacement $H'_{\mathrm{II}}(k_y \to k_x, k_z)$ in Eq. (9). An electron wave packet is injected from the local lead at $\boldsymbol{r}_i = (-x_i, 0)$ on surface I, then transmitted to surface II via negative refraction, and finally reaches the tip of the scanning tunneling microscope (STM) at $\boldsymbol{r}_f = (x_f, 0)$. The wave packet propagates along a spatially localized trajectory [see Fig. 1(c)]. This behavior can be revealed by the appearance of a peak structure in the spatially resolved nonlocal conductance as a function of x_f [calculated below; see Fig. 2(c)]. Crucially, this signature is unique to the negative refraction through the Fermi arc surface states. For normal-metal states, the conductance decays with x_f, as the wave packet expands in the z direction.

In the following, we calculate the nonlocal conductance using the surface Hamiltonian (9) and the Green's function method. The Fermi energy is set to zero for simplicity, so that bulk electrons do not contribute to the conductivity. The finite density of the bulk states can solely lead to leakage of electrons, which will not change our main results. The coupling between the terminals and the surface states is described by a tunneling Hamiltonian as

$$H_T = \sum_{p,\alpha=i,f} T_\alpha d^\dagger_{p,\alpha} \Psi(\boldsymbol{r}_\alpha) + \mathrm{H.c.}, \tag{10}$$

where T_α is the tunneling strength between the system and the α terminal, $d_{p,\alpha}$ is the Fermi operator in the α terminal with momentum p, and $\Psi(\boldsymbol{r})$ is the field operator of the surface states at position $\boldsymbol{r}$, with $\boldsymbol{r}_\alpha$ corresponding to each terminal location.

The nonlocal conductance (including spin degeneracy) between the local electrode and the STM tip is given by [52]

$$\sigma(\varepsilon) = \frac{2e^2}{h} \mathrm{Tr}[\Gamma_i G^R \Gamma_f G^A]. \tag{11}$$

The full retarded (R) and advanced (A) Green's function $G^{R,A}$ and the linewidth functions Γ_α are (see Appendix C for details)

$$G^{R,A}_\varepsilon(\boldsymbol{r}_f, \boldsymbol{r}_i) = (1 + R_i)^{-1} g^{R,A}_\varepsilon(\boldsymbol{r}_f, \boldsymbol{r}_i)(1 + R_f)^{-1}, \tag{12}$$

$$\Gamma_\alpha(\boldsymbol{r}_1, \boldsymbol{r}_2, \varepsilon) = 2\pi \rho_\alpha(\varepsilon) |T_\alpha|^2 \delta(\boldsymbol{r}_1 - \boldsymbol{r}_\alpha)\delta(\boldsymbol{r}_2 - \boldsymbol{r}_\alpha), \tag{13}$$

where the function $R_\alpha(\varepsilon) = \pi^2 \rho_0(\varepsilon)\rho_\alpha(\varepsilon)|T_\alpha|^2$, with $\rho_0(\varepsilon) = k_0/(2\pi^2\hbar v)$ being the density of states (DOS) of Fermi arc surface states per unit area and $\rho_\alpha(\varepsilon)$ being the DOS of the terminal α at energy ε. The bare Green's function is [see Eq. (C2)]

$$g^R_\varepsilon(\boldsymbol{r}_f, \boldsymbol{r}_i) = \left[g^A_\varepsilon(\boldsymbol{r}_i, \boldsymbol{r}_f)\right]^* = -2\pi i \rho_0(\varepsilon) f_\varepsilon(\boldsymbol{r}_f, \boldsymbol{r}_i), \tag{14}$$

with

$$f_\varepsilon(\boldsymbol{r}_f, \boldsymbol{r}_i) = \int_{-k_0\cos\varphi}^{k_0\cos\varphi} dk_z \frac{e^{i(k_{x2}x_f - k_x x_i)}}{2k_0\cos\varphi} e^{ik_z(z_f - z_i)}. \tag{15}$$

Here, k_x and k_{x2} are solved by $H'_{\mathrm{I}}(k_x, k_z) = \varepsilon$ and $H'_{\mathrm{II}}(k_{x2}, k_z) = \varepsilon$, respectively. The interval of integration covers the Fermi arc region, and the k_z dependence of the velocity in the x direction is ignored.

Performing integration in Eq. (11) yields

$$\sigma(\varepsilon) = \sigma_0(\varepsilon)|f_\varepsilon(\boldsymbol{r}_f, \boldsymbol{r}_i)|^2, \tag{16}$$

$$\sigma_0(\varepsilon) = \frac{32e^2}{h} \frac{R_i}{(1 + R_i)^2} \frac{R_f}{(1 + R_f)^2}, \tag{17}$$

where σ_0 takes the maximum value $2e^2/h$ when $R_i = R_f = 1$. The dependence of $\sigma(\varepsilon)$ on x_f comes from the factor $|f_\varepsilon(\boldsymbol{r}_f, \boldsymbol{r}_i)|^2$, which has a peak due to negative refraction [see Fig. 2(c)]. In particular, when $\varepsilon = 0$, $k_{x2}(\varepsilon, k_z) = -k_x(\varepsilon, k_z)$, one can see from Eq. (15) that the peak of the function $|f_\varepsilon(\boldsymbol{r}_f, \boldsymbol{r}_i)|^2$ is centered around $x_f = x_i$ on the x axis. The peak structure in the nonlocal conductance stems from the wave packet trajectory of negative refraction in Fig. 1(c). The width of the peak w, corresponding to the scale of the wave packet, is comparable to π/k_0, which can be seen from Eq. (15). Specifically, in the case of straight Fermi arcs and $\varepsilon = 0$, we will have $k_{x2} = -k_x = k_z$. Performing the integration in Eq. (15) yields $f_{\varepsilon=0}(\boldsymbol{r}_f, \boldsymbol{r}_i) = \sin[k_0(x_i + x_f)\cos\varphi]/[k_0(x_i +$

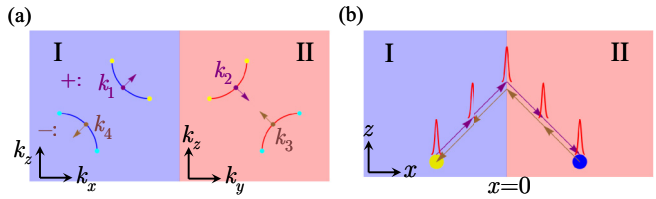

FIG. 3. Negative refraction between multiple Fermi arcs at different surfaces of Weyl semimetals. (a) Effective surface model for a $\mathcal{T}$-symmetric Weyl semimetal. There are two branches of Fermi arcs with opposite chirality (labeled + and −). (b) Fabry-Pérot interference led by backscattering at the terminals (blue and gold disks).

$x_f)\cos\varphi]$; thus, the peak width for $|f_{\varepsilon=0}(\boldsymbol{r}_f,\boldsymbol{r}_i)|^2$ is comparable to π/k_0. For curved Fermi arcs with dispersion ($d\neq 0$), the wave packet spreads during its propagation, so that the peak of conductance is broadened as well [see Fig. 2(c)]. Therefore, the peak width w provides useful information about the length of the Fermi arcs. The existence of the peak structure is also confirmed numerically in Fig. 7(a).

IV. NEGATIVE REFRACTION IN $\mathcal{T}$-SYMMETRIC WEYL SEMIMETALS

In reality, there are only a few material candidates for Weyl semimetals with only two Weyl points [42–44]. Hence, we investigate negative refraction between the surface states of $\mathcal{T}$-symmetric Weyl semimetals, which are more abundant [12–16]. Specifically, we study a semimetal with four Weyl points. Our results can be readily extended to the situation with more Weyl points.

Consider a $\mathcal{T}$-symmetric Weyl semimetal with two pairs of Weyl points. Correspondingly, there are two Fermi arc segments on each open surface, which are the time-reversal counterparts to each other [see Fig. 3(a)]. The existence of two branches of surface states with opposite chiralities enables backscattering between them. For simplicity, we restrict our discussion to the case in which two Fermi arcs on the same surface do not overlap when projecting to the k_z axis. This means that no backscattering occurs for conserved k_z, so that perfect negative refraction occurs at the interface between surfaces I and II [41]. However, backscattering takes place at the local terminals, leading to Fabry-Pérot interference [Fig. 3(b)] and additional oscillation of the nonlocal conductance on top of the peak structure in real space.

More concretely, the two adjacent open surfaces I and II contain two Fermi arcs each, as shown in Fig. 3(a). We describe branch + by

$$H_+(k_x,k_z)=\begin{cases}H'_{\rm I}(k_x-k_{x_0},k_z-k_{z_0}) & x<0,\\ H'_{\rm II}(k_x+k_{x_0},k_z-k_{z_0}) & x>0,\end{cases} \tag{18}$$

which is similar to Eq. (9) except for a shift of the Fermi arcs in the surface Brillouin zone. The time-reversal counterpart, branch −, is described by $H_-(k_x,k_z)=H_+(-k_x,-k_z)$.

Like for the $\mathcal{P}$-symmetric case, we first solve the Green's function for the surface states, yielding

$$\tilde{g}^R_\varepsilon(\boldsymbol{r}_f,\boldsymbol{r}_i)=\tilde{g}^R_\varepsilon(\boldsymbol{r}_i,\boldsymbol{r}_f)=-\pi i\rho'_0(\varepsilon)f'_\varepsilon(\boldsymbol{r}_f,\boldsymbol{r}_i), \tag{19}$$

with

$$f'_\varepsilon(\boldsymbol{r}_f,\boldsymbol{r}_i)=\int_{k_1^+}^{k_2^+}dk_z\frac{e^{i(k'_{x2}x_f-k'_x x_i)}}{k_2^+-k_1^+}e^{ik_z(z_f-z_i)}, \tag{20}$$

where $\rho'_0(\varepsilon)$ is the density of surface states per unit area and k_1^+ and k_2^+ are the k_z components of the terminations of the Fermi arcs in branch +. k'_x and k'_{x2} are solved by $H'_{\rm I}(k'_x-k_{x_0},k_z-k_{z_0})=\varepsilon$ and $H'_{\rm II}(k'_{x2}+k_{x_0},k_z-k_{z_0})=\varepsilon$, respectively. We describe the coupling to the terminals by the same tunneling Hamiltonian (10), which leads to the same self-energy in Eq. (C3). The full Green's function, however,

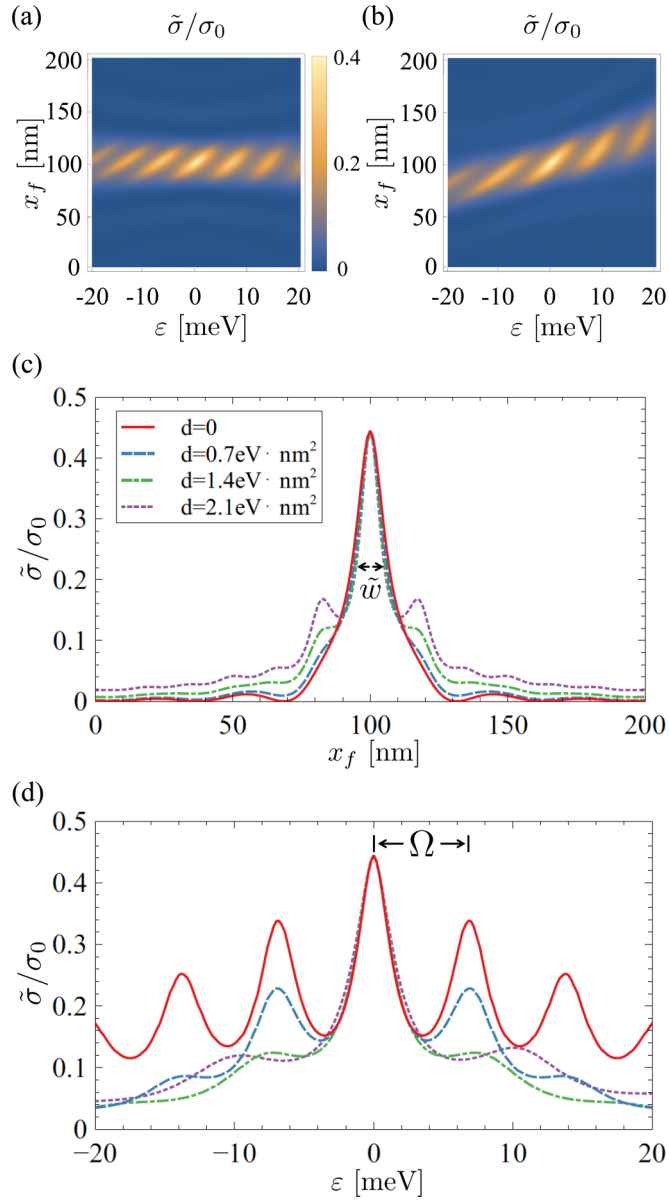

FIG. 4. Nonlocal conductance $\tilde{\sigma}(\varepsilon)$ in a $\mathcal{T}$-symmetric Weyl semimetal [see Eq. (18)] with (a) straight ($d=0$) and (b) curved Fermi arcs ($d=0.7\,\mathrm{eV\,nm^2}$). The dependence of the conductance on (c) x_f for fixed $\varepsilon=0$ and (d) ε with $x_f=x_i$ for Fermi arcs with different curvatures [labeled by the legend in (c)]. Parameters are $R_i=R_f=1$, $k_0=0.2\,\mathrm{nm^{-1}}$, and $k_{x_0}=k_{z_0}=k_0/\sqrt{2}$, and other parameters are the same as those in Fig. 2.

takes a different form due to the backscattering at the terminals,

$$\tilde{G}^R_\varepsilon(\boldsymbol{r}_f,\boldsymbol{r}_i)=\frac{\tilde{g}^R_\varepsilon(\boldsymbol{r}_f,\boldsymbol{r}_i)}{(1+R_i)(1+R_f)-R_iR_f f'^2_\varepsilon(\boldsymbol{r}_f,\boldsymbol{r}_i)}. \quad (21)$$

The resulting nonlocal conductance calculated by Eq. (11) is

$$\tilde{\sigma}(\varepsilon)=\frac{\sigma_0}{4}\left|\frac{f'_\varepsilon(\boldsymbol{r}_f,\boldsymbol{r}_i)}{1-R_iR_f f'^2_\varepsilon(\boldsymbol{r}_f,\boldsymbol{r}_i)/[(1+R_i)(1+R_f)]}\right|^2, \quad (22)$$

which differs from the $\mathcal{P}$-symmetric Weyl semimetal [see Eq. (16)] mainly by the additional term in the denominator due to the multiple scattering in Fig. 3(b). In the weak tunneling limit $R_{i,f}\ll 1$, the effect due to multiple scattering is negligible, and the conductance $\tilde{\sigma}(\varepsilon)\approx\frac{\sigma_0}{4}|f'_\varepsilon(\boldsymbol{r}_f,\boldsymbol{r}_i)|^2$. More generally, the conductance as a function of energy and x_f is plotted in Figs. 4(a) and 4(b). The nonlocal conductance displays additional Fabry-Pérot oscillations induced by multiple scattering on top of the peak structure in real space, resulting in the appearance of side peaks for large dispersion d [see Fig. 4(c)], which is verified by numerical simulations using a lattice model in Fig. 7(b). The width of the main peak $\tilde{w}$ is comparable to $\pi/(k_2^+-k_1^+)$ for the same reason as in the $\mathcal{P}$-symmetric case. The Fabry-Pérot interference also results in oscillation of conductance with energy when d is small [Figs. 4(a) and 4(d)], which is due to the dependence of the Fermi momenta on energy. Specifically, assume that, for branch +, the Fermi velocity along the x direction $v_{x,+}$ (see Fig. 3) is independent of k_z. This implies that when the energy increases by $\Delta\varepsilon$, the momenta k'_x and k'_{x2} will increase by $\Delta\varepsilon/v_{x,+}$. Therefore, the function $f'_\varepsilon(\boldsymbol{r}_f,\boldsymbol{r}_i)$ [see Eq. (20)] gains an additional phase factor of $\Delta\varepsilon(x_f-x_i)/v_{x,+}$. Due to the factor $f'_\varepsilon(\boldsymbol{r}_f,\boldsymbol{r}_i)^2$ in the denominator of Eq. (22), the oscillation period with ε, denoted by Ω in Fig. 4(d), is comparable to $\pi v_{x,+}/(x_f-x_i)$. Note that, in the case of large d, the center of the resonant peak in real space moves with ε [Fig. 4(b)], and oscillation with ε cannot be seen due to the rapid decrease of the conductance at $\varepsilon\neq 0$ [Fig. 4(d)].

V. DISCUSSION AND CONCLUSION

So far, we have analyzed negative refraction based on the minimal model of $\mathcal{P}$- and $\mathcal{T}$-symmetric Weyl semimetals. Several important issues related to the experimental implementation of our proposal are discussed in the following.

(i) Our scheme applies also to polyhedral nanowires with N surfaces. When the Weyl nodes are aligned in a direction deviating from the central axis, the Fermi arcs on the surfaces become tilted, and many refraction processes take place at the boundary of the facets, as shown in Fig. 5. While many of the refraction processes are normal refraction, one of them is negative refraction, which leads to a spatially localized trajectory similar to Fig. 1(c). The scheme should also hold at $N\to\infty$, when the polyhedron becomes a cylinder.

(ii) For Weyl semimetals with more Weyl points and Fermi arcs than those obtained within the minimal model, as in most materials [12–23], our main results still hold as long as the overlap between the projections of different incident and reflection channels with conserved momentum k_z is negligibly small. In this case, due to the different orientations of Fermi arcs and the corresponding trajectories of negative refraction,

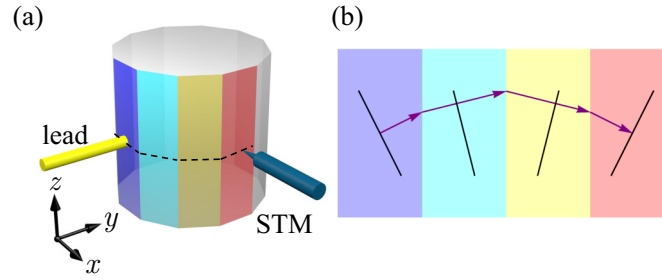

FIG. 5. (a) Sketch of the setup of nonlocal conductance measurement in the case of a polyhedral nanowire. (b) Tilted Fermi arcs (black lines) result in a spatially localized trajectory (purple arrows) where negative refraction takes place on one of the interfaces. Such a localized trajectory leads to a peak structure in nonlocal conductance similar to Figs. 2 and 4.

a multiple-peak structure in the nonlocal conductance may appear in the same transport scheme in Fig. 2(a). The negative refraction will get suppressed if the overlap between the projections of the incident and reflection Fermi arcs is large due to the enhanced backscattering.

(iii) We considered Fermi arcs with a regular shape, such that electrons propagate on the surfaces towards certain directions, which is the main difference between Fermi arc states and normal-metal states. For Weyl semimetals with long and winding Fermi arcs, surface transport will occur in different directions similar to normal metals, and negative refraction cannot be observed.

(iv) In real materials, the Fermi energy usually deviates from the Weyl points, resulting in a finite density of bulk states. Our result is not sensitive to such a deviation because the nonlocal transport occurs on the surface of the sample. The bulk states only lead to certain leakage of the injected electrons, and these leaked electrons do not follow the trajectory of negative refraction. As a result, their propagation does not have a peak structure in real space, and they contribute only a small background to the conductance peak in the nonlocal transport. Such a small background will not change the qualitative results.

(v) By using Eqs. (2) and (3) as effective descriptions of the Fermi arc surface states we ignore the penetration of the surface states into the bulk. This is because in most intervals between the Weyl nodes the surface states are well localized on the surface. Only in the vicinity of Weyl points will the surface states possess a long penetration into the bulk. These states are not much different from the bulk states and will not kill the signature of negative refraction, as discussed in point (iv). Another effect of such penetration is that it effectively reduces the available transport channels on the surface or, equivalently, the length of the Fermi arcs, which also does not change the main results.

(vi) Finally, surface imperfections such as dangling bonds may exist, which can be treated as disorder. In $\mathcal{P}$-symmetric Weyl semimetals, such surface disorder should have little effect on the negative refraction, and the conductance peak remains stable. This is because the surface states are unidirectional and are thus immune to backscattering. However, in $\mathcal{T}$-symmetric Weyl semimetals surface disorder will lead

to backscattering between the time-reversal counterpart of the Fermi arcs with opposite chirality, which reduces the negative refraction efficiency as well as the peak structure of the nonlocal conductance.

In summary, we have shown that perfect negative refraction, which can be realized on two adjacent surfaces of Weyl semimetals with properly oriented Fermi arcs, leads to distinct spatial trajectories for electron propagation. The space-resolved peak structure of the nonlocal conductance which indicates the trajectory of negative refraction can serve as unique evidence of the Fermi arc states. Recent progress on Weyl semimetals with a single pair of Weyl nodes in $MnBi_2Te_4$ [42] and $EuCd_2As_2$ [43,44] paves the way for the realization of our proposal. Furthermore, the manipulation of the negative refraction process offers potential applications of a Weyl semimetal nanowire as a field-effect transistor [40]. Our work opens a platform to study negative refraction in electronics [47–50]. Compared with the existing physical systems, the negative refraction in Fermi arc states exhibits an unambiguous signature for its detection.

ACKNOWLEDGMENTS

We acknowledge financial support from the Swiss National Science Foundation (SNSF) through Division II and the Careers Division. We would like to thank J. L. Lado for helpful discussions.

APPENDIX A: DERIVATION OF FERMI ARC STATES

We derive the Fermi arc surface state at an open surface in the $-y$ direction [Eq. (2)] in the Weyl semimetal [Eq. (1)]. The surface state at the open surface in the x direction can be obtained similarly. To calculate the surface state we make the substitution $k_y \to -i\partial_y$ to the Hamiltonian Eq. (1) since the existence of the open surface breaks translational symmetry in the y direction. Thus, the surface state $\psi(k_x, y, k_z)$ satisfies the following equation:

$$[H(k_x, -i\partial_y, k_z) - E]\psi(k_x, y, k_z) = 0, \tag{A1}$$

with boundary conditions

$$\psi(k_x, y = 0, k_z) = \psi(k_x, y = +\infty, k_z) = 0. \tag{A2}$$

Expanding $\psi(k_x, y, k_z) = \sum_\lambda a_\lambda \psi_\lambda$ on the basis

$$\psi_\lambda(k_x, y, k_z) = e^{ik_x x + ik_z z} e^{\lambda y} \begin{pmatrix} a \\ b \end{pmatrix}, \tag{A3}$$

where a and b are the pseudospin components of $\psi(k_x, y, k_z)$, and substituting into Eq. (A1), we have $a_\lambda \neq 0$ only for

$$[H(k_x, -i\lambda, k_z) - E]\begin{pmatrix} a \\ b \end{pmatrix} = 0. \tag{A4}$$

Equation (A4) implies that

$$H^2 = \hbar^2 v^2 \left(k_x^2 - \lambda^2\right) + M^2(\lambda^2 - F)^2 = E^2, \tag{A5}$$

where $F = k_x^2 + k_z^2 - k_0^2$, yielding two possible solutions of λ^2:

$$\lambda^2 = F + \frac{\hbar^2 v^2 \pm \sqrt{4M^2 F_2 + \hbar^4 v^4}}{2M^2}, \tag{A6}$$

with $F_2 = E^2 + \hbar^2 v^2 (F - k_x^2)$. Among all possible linear combinations of ψ_λ with λ satisfying Eq. (A6), the only one that satisfies the boundary conditions (A2) is

$$\psi(k_x, y, k_z) = e^{ik_x x + ik_z z}(e^{\lambda_1 y} - e^{\lambda_2 y})\begin{pmatrix} a \\ b \end{pmatrix}, \tag{A7}$$

with $\lambda_2 < \lambda_1 < 0$. To get the dispersion of the eigenstate (A7), note that

$$-\frac{a}{b} = \frac{\hbar v(k_x - \lambda_1)}{M\left(\lambda_1^2 - F\right) - E} = \frac{\hbar v(k_x - \lambda_2)}{M\left(\lambda_2^2 - F\right) - E}. \tag{A8}$$

The self-consistent solution to Eqs. (A6) and (A8) is

$$E = \mathrm{sgn}(M)\hbar v k_x, \tag{A9}$$

with sgn being the sign function.

APPENDIX B: NUMERICAL CALCULATION OF FERMI ARCS

In this Appendix, we verify numerically that for the $\mathcal{P}$- and $\mathcal{T}$- symmetric Weyl semimetals [see Eq. (1)], rotation of the effective bulk model leads to the oriented Fermi arcs on open surfaces.

For the $\mathcal{P}$-symmetric Weyl semimetal we adopt the effective model $H'(\boldsymbol{k})$ in the main text. For the $\mathcal{T}$-symmetric Weyl semimetal, we start with a minimal model

$$H_{\mathrm{TR}}(\boldsymbol{k}) = M\left(k_1^2 - k_x^2\right)\sigma_x + \hbar v k_y \sigma_y + M\left(k_0^2 - k_y^2 - k_z^2\right)\sigma_z, \tag{B1}$$

which has two Fermi arcs on each open surface. Then, we perform the rotational transformation to the effective Hamiltonian to obtain generally orientated Fermi arcs as $H'_{\mathrm{TR}}(\boldsymbol{k}) = H_{\mathrm{TR}}(\tilde{U}^{-1}\boldsymbol{k})$, with

$$\tilde{U}(\phi) = \begin{pmatrix} \frac{\cos\phi}{\sqrt{2}} & \frac{1}{\sqrt{2}} & -\frac{\sin\phi}{\sqrt{2}} \\ -\frac{\cos\phi}{\sqrt{2}} & \frac{1}{\sqrt{2}} & \frac{\sin\phi}{\sqrt{2}} \\ \sin\phi & 0 & \cos\phi \end{pmatrix}. \tag{B2}$$

The reason we apply $\tilde{U}(\phi)$ instead of $U(\varphi)$ [see Eq. (4)] in the $\mathcal{T}$-symmetric case is because of different original positions of the Weyl points in the Brillouin zone compared to the $\mathcal{P}$-symmetric case.

In the long-wavelength limit, the matching lattice model used in the numerical simulation can be constructed from the effective Hamiltonian through the substitution $k_{i=x,y,z} \to a^{-1}\sin k_i a$, $\quad k_i^2 \to 2a^{-2}(1 - \cos k_i a)$, where a is the lattice constant. The Fermi arcs of the $\mathcal{P}$-symmetric Weyl semimetal with $\varphi = \cos^{-1}\frac{1}{\sqrt{3}}$ (such that $\theta = \frac{\pi}{4}$) and $\mathcal{T}$-symmetric Weyl semimetal with $\phi = \frac{\pi}{4}$ are shown in Fig. 6.

APPENDIX C: GREEN'S FUNCTION CALCULATION

For a fixed energy E, the normalized eigenstate of the surface Hamiltonian is

$$\psi_{k_z,E}(x, z) = \frac{e^{ik_z z}}{\sqrt{S}}[\theta(-x)e^{ik_x x} + \theta(x)e^{ik_{x2} x}], \tag{C1}$$

where the momentum k_z is conserved during the transmission and k_x and k_{x2} are solved by $H'_{\mathrm{I}}(k_x, k_z) = E$ and $H'_{\mathrm{II}}(k_{x2}, k_z) =$

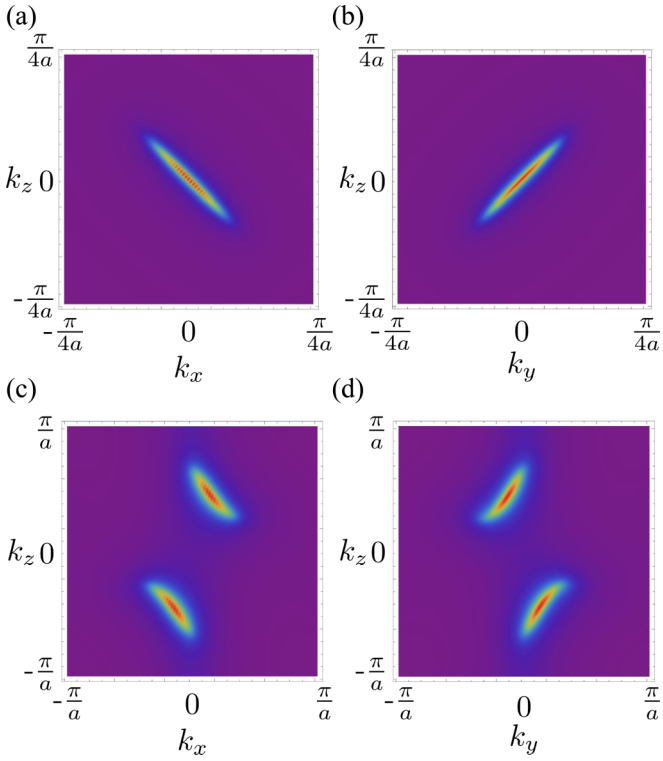

FIG. 6. Fermi arcs on surfaces (a) I and (b) II of $H'(\boldsymbol{k})$ and those on surfaces (c) I and (d) II of $H'_{\mathrm{TR}}(\boldsymbol{k})$, with parameters $k_0 = 0.1\,\mathrm{nm}^{-1}$, $M = -1.25\,\mathrm{eV\,nm}^2$, and $\varphi = \cos^{-1}\frac{1}{\sqrt{3}}$ in $H'(\boldsymbol{k})$ and $k_0 = 0.2\,\mathrm{nm}^{-1}$, $k_1 = \sqrt{2}k_0$, $M = 1.25\,\mathrm{eV\,nm}^2$, and $\phi = \frac{\pi}{4}$ in $H'_{\mathrm{TR}}(\boldsymbol{k})$.

E, respectively. The function $\theta(\pm x)$ is the Heaviside step function defining the two sides of the junction, and S is the combined area of surfaces I and II. Without coupling to the terminals, the bare Green's functions can be constructed as

$$g_{\varepsilon}^{R,A}(\boldsymbol{r}_f, \boldsymbol{r}_i) = \sum_E \sum_{k_z} \frac{\psi_{k_z,E}(\boldsymbol{r}_f)\psi^*_{k_z,E}(\boldsymbol{r}_i)}{\varepsilon - E \pm i0}, \tag{C2}$$

thus describing electron propagation from $\boldsymbol{r}_i$ to $\boldsymbol{r}_f$. Since the surface states are unidirectional, we have $g_{\varepsilon}^{R}(\boldsymbol{r}_i, \boldsymbol{r}_f) = 0$. By writing the sums as integrals we obtain Eq. (14) in the main text.

The coupling to the α terminal introduces finite self-energy to the Green's function of the surface state as

$$\Sigma_{\alpha}^{R}(\boldsymbol{r}_1, \boldsymbol{r}_2, \varepsilon) = -i\pi\,\rho_{\alpha}(\varepsilon)|T_{\alpha}|^2\delta(\boldsymbol{r}_1 - \boldsymbol{r}_{\alpha})\delta(\boldsymbol{r}_2 - \boldsymbol{r}_{\alpha}). \tag{C3}$$

The full Green's function can be calculated by Dyson's equation, which yields Eq. (12) in the main text. The linewidth function is defined by $\Gamma_{\alpha}(\boldsymbol{r}_1 - \boldsymbol{r}_{\alpha}) = 2i\Sigma_{\alpha}^{R}(\boldsymbol{r}_1 - \boldsymbol{r}_{\alpha})$, corresponding to Eq. (13) in the main text.

APPENDIX D: NUMERICAL SIMULATIONS OF THE NONLOCAL TRANSPORT EXPERIMENT

We compare our semiclassical analytical calculation approach with numerical simulations of the nonlocal transport experiment for both $\mathcal{P}$- and $\mathcal{T}$-symmetric Weyl semimetals $H'(\boldsymbol{k})$ and $H'_{\mathrm{TR}}(\boldsymbol{k})$ using the numerical package KWANT [53]. To be realistic, we adopt on-site potential U_{I} (U_{II}) on the first layer of the lattice on surface I (II) to introduce dispersion effects, which results in curved Fermi arcs. The nonlocal conductance under different choices of the on-site potentials $U_{\mathrm{I,II}}$ is shown in Fig. 7. In both cases, the conductance peak value increases with the on-site potential, which is due to the increase of the surface DOS. In addition, in the $\mathcal{T}$-symmetric case, the position of the peak varies for different on-site potentials, which is due to the shift of the phase term in $f'_{\varepsilon}(\boldsymbol{r}_f, \boldsymbol{r}_i)$ for dispersive Fermi arcs. In both cases, the peak structure persists for dispersive Fermi arcs, in agreement with the analytical results in Figs. 2 and 4.

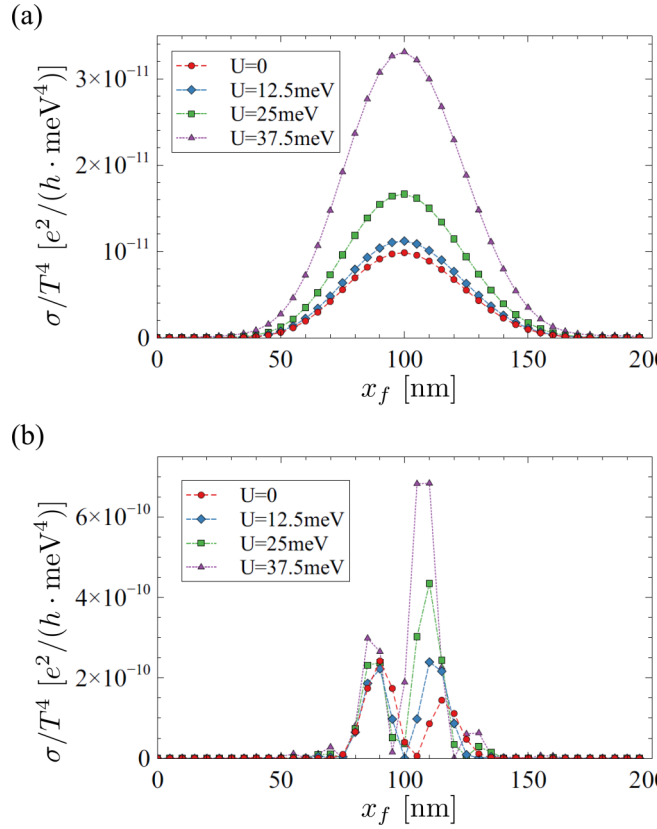

FIG. 7. Numerical simulations of nonlocal conductance for (a) $\mathcal{P}$-symmetric Weyl semimetal $H'(\boldsymbol{k})$ with different dispersions $U_{\mathrm{I}} = -U_{\mathrm{II}} = U$ and (b) $\mathcal{T}$-symmetric Weyl semimetal $H'_{\mathrm{TR}}(\boldsymbol{k})$ with different dispersions $U_{\mathrm{I}} = U_{\mathrm{II}} = -U$. The setup is the same as the one shown in Fig. 2(a), with the scattering region being a Weyl nanowire with a cross section of 40×40 sites with lattice constant $a = 5$ nm. The conductance is normalized by T^4, with T being the tunneling between the leads and the nanowire [see Eq. (10)]. In realistic cases, T is determined by the hopping between the leads and the system as well as the DOS of the system. Parameters are $v = 10^6$ m/s, $x_i = 100$ nm, and $\varepsilon = 0$, and all other parameters are the same as in Fig. 6.

APPENDIX E: INTRODUCTION OF SURFACE DISPERSION FROM ON-SITE POTENTIAL

We show explicitly that the on-site potentials U_{I} (U_{II}) we adopt on the surface of the Weyl semimetal in Appendix D result in the dispersion terms in Eq. (9). Note that the surface states on surface I possess a **k**-dependent

wave function $\psi_{k_x,k_z}(y)$ that has some spatial profile along the y direction. Under surface potential $U_{\rm I}(y)$, the potential that the states feel can be evaluated by the overlap integral $U_{\rm I}(k) = \int_0^\infty U_{\rm I}(y)|\psi_{k_x,k_z}(y)|^2 dy$, which is **k** dependent and thus serves as an effective dispersion $\varepsilon_{\rm I}(k_x, k_z) = U_{\rm I}(k_x, k_z)$. In our model, the surface states' wave functions satisfy $|\psi_{k_x,k_z}(y)| = |\psi_{-k_x,-k_z}(y)|$ so that the effective dispersion is an even function of k_x and k_z and takes the form $\varepsilon_y(k_x, k_z) = \varepsilon_0 - d(k_x^2 + k_z^2)$ to second order in k_x and k_z. In addition, the dispersion term should vanish at Weyl points where the surface states spread in the whole bulk, which leads to $\varepsilon_0 = d(1 - \sin^2\varphi/2)k_0^2$. Therefore, the surface potential $U_{\rm I}$ leads to the dispersion ε_x in Eq. (9). Similarly, the surface potential $U_{\rm II}$ leads to the dispersion ε_y in Eq. (9)

[1] M. Z. Hasan and C. L. Kane, Rev. Mod. Phys. **82**, 3045 (2010).
[2] X.-L. Qi and S.-C. Zhang, Rev. Mod. Phys. **83**, 1057 (2011).
[3] N. P. Armitage, E. J. Mele, and A. Vishwanath, Rev. Mod. Phys. **90**, 015001 (2018).
[4] C. Fang, H. Weng, X. Dai, and Z. Fang, Chin. Phys. B **25**, 117106 (2016).
[5] X. Wan, A. M. Turner, A. Vishwanath, and S. Y. Savrasov, Phys. Rev. B **83**, 205101 (2011).
[6] S. Murakami, New J. Phys. **9**, 356 (2007).
[7] A. A. Burkov and L. Balents, Phys. Rev. Lett. **107**, 127205 (2011).
[8] Z. Wang, H. Weng, Q. Wu, X. Dai, and Z. Fang, Phys. Rev. B **88**, 125427 (2013).
[9] H. Weng, C. Fang, Z. Fang, B. A. Bernevig, and X. Dai, Phys. Rev. X **5**, 011029 (2015).
[10] S.-M. Huang, S.-Y. Xu, I. Belopolski, C.-C. Lee, G. Chang, B. Wang, N. Alidoust, G. Bian, M. Neupane, C. Zhang *et al.*, Nat. Commun. **6**, 7373 (2015).
[11] A. A. Burkov, M. D. Hook, and L. Balents, Phys. Rev. B **84**, 235126 (2011).
[12] B. Q. Lv, H. M. Weng, B. B. Fu, X. P. Wang, H. Miao, J. Ma, P. Richard, X. C. Huang, L. X. Zhao, G. F. Chen, Z. Fang, X. Dai, T. Qian, and H. Ding, Phys. Rev. X **5**, 031013 (2015).
[13] S.-Y. Xu, I. Belopolski, N. Alidoust, M. Neupane, G. Bian, C. Zhang, R. Sankar, G. Chang, Z. Yuan, C.-C. Lee *et al.*, Science **349**, 613 (2015).
[14] S.-Y. Xu, N. Alidoust, I. Belopolski, Z. Yuan, G. Bian, T.-R. Chang, H. Zheng, V. N. Strocov, D. S. Sanchez, G. Chang *et al.*, Nat. Phys. **11**, 748 (2015).
[15] S.-Y. Xu, I. Belopolski, D. S. Sanchez, C. Zhang, G. Chang, C. Guo, G. Bian, Z. Yuan, H. Lu, T.-R. Chang *et al.*, Sci. Adv. **1**, e1501092 (2015).
[16] N. Xu, H. Weng, B. Lv, C. E. Matt, J. Park, F. Bisti, V. N. Strocov, D. Gawryluk, E. Pomjakushina, K. Conder *et al.*, Nat. Commun. **7**, 11006 (2016).
[17] K. Deng, G. Wan, P. Deng, K. Zhang, S. Ding, E. Wang, M. Yan, H. Huang, H. Zhang, Z. Xu *et al.*, Nat. Phys. **12**, 1105 (2016).
[18] L. Yang, Z. Liu, Y. Sun, H. Peng, H. Yang, T. Zhang, B. Zhou, Y. Zhang, Y. Guo, M. Rahn *et al.*, Nat. Phys. **11**, 728 (2015).
[19] L. Huang, T. M. McCormick, M. Ochi, Z. Zhao, M.-T. Suzuki, R. Arita, Y. Wu, D. Mou, H. Cao, J. Yan *et al.*, Nat. Mater. **15**, 1155 (2016).
[20] A. Tamai, Q. S. Wu, I. Cucchi, F. Y. Bruno, S. Riccò, T. K. Kim, M. Hoesch, C. Barreteau, E. Giannini, C. Besnard, A. A. Soluyanov, and F. Baumberger, Phys. Rev. X **6**, 031021 (2016).
[21] J. Jiang, Z. Liu, Y. Sun, H. Yang, C. Rajamathi, Y. Qi, L. Yang, C. Chen, H. Peng, C. Hwang *et al.*, Nat. Commun. **8**, 13973 (2017).
[22] I. Belopolski, D. S. Sanchez, Y. Ishida, X. Pan, P. Yu, S.-Y. Xu, G. Chang, T.-R. Chang, H. Zheng, N. Alidoust *et al.*, Nat. Commun. **7**, 13643 (2016).
[23] B. Lv, N. Xu, H. Weng, J. Ma, P. Richard, X. Huang, L. Zhao, G. Chen, C. Matt, F. Bisti *et al.*, Nat. Phys. **11**, 724 (2015).
[24] W. Chen, K. Luo, L. Li, and O. Zilberberg, Phys. Rev. Lett. **121**, 166802 (2018).
[25] W. Chen and J. L. Lado, Phys. Rev. Lett. **122**, 016803 (2019).
[26] L. Lu, L. Fu, J. D. Joannopoulos, and M. Soljačić, Nat. Photonics **7**, 294 (2013).
[27] L. Lu, Z. Wang, D. Ye, L. Ran, L. Fu, J. D. Joannopoulos, and M. Soljačić, Science **349**, 622 (2015).
[28] M. Xiao, W.-J. Chen, W.-Y. He, and C. T. Chan, Nat. Phys. **11**, 920 (2015).
[29] Z. Yang and B. Zhang, Phys. Rev. Lett. **117**, 224301 (2016).
[30] C. H. Lee, S. Imhof, C. Berger, F. Bayer, J. Brehm, L. W. Molenkamp, T. Kiessling, and R. Thomale, Commun. Phys. **1**, 39 (2018).
[31] K. Luo, R. Yu, H. Weng *et al.*, Research **2018**, 6793752 (2018).
[32] Y. Lu, N. Jia, L. Su, C. Owens, G. Juzeliūnas, D. I. Schuster, and J. Simon, Phys. Rev. B **99**, 020302(R) (2019).
[33] L. Balents, Physics **4**, 36 (2011).
[34] K.-Y. Yang, Y.-M. Lu, and Y. Ran, Phys. Rev. B **84**, 075129 (2011).
[35] P. J. Moll, N. L. Nair, T. Helm, A. C. Potter, I. Kimchi, A. Vishwanath, and J. G. Analytis, Nature (London) **535**, 266 (2016).
[36] L.-X. Wang, C.-Z. Li, D.-P. Yu, and Z.-M. Liao, Nat. Commun. **7**, 10769 (2016).
[37] N. Bovenzi, M. Breitkreiz, P. Baireuther, T. E. O'Brien, J. Tworzydło, İ. Adagideli, and C. W. J. Beenakker, Phys. Rev. B **96**, 035437 (2017).
[38] Z. Faraei and S. A. Jafari, Phys. Rev. B **100**, 035447 (2019).
[39] F. Adinehvand, Z. Faraei, T. Farajollahpour, and S. A. Jafari, Phys. Rev. B **100**, 195408 (2019).
[40] G. Chen, W. Chen, and O. Zilberberg, APL Mater. **8**, 011102 (2020).
[41] H. He, C. Qiu, L. Ye, X. Cai, X. Fan, M. Ke, F. Zhang, and Z. Liu, Nature (London) **560**, 61 (2018).
[42] J. Li, Y. Li, S. Du, Z. Wang, B.-L. Gu, S.-C. Zhang, K. He, W. Duan, and Y. Xu, Sci. Adv. **5**, eaaw5685 (2019).
[43] L.-L. Wang, N. H. Jo, B. Kuthanazhi, Y. Wu, R. J. McQueeney, A. Kaminski, and P. C. Canfield, Phys. Rev. B **99**, 245147 (2019).
[44] J.-R. Soh, F. de Juan, M. Vergniory, N. Schröter, M. Rahn, D. Yan, M. Bristow, P. A. Reiss, J. N. Blandy, Y. F. Guo *et al.*, Phys. Rev. B **100**, 201102(R) (2019).

[45] N. Morali, R. Batabyal, P. K. Nag, E. Liu, Q. Xu, Y. Sun, B. Yan, C. Felser, N. Avraham, and H. Beidenkopf, Science **365**, 1286 (2019).

[46] H. Yang, L. Yang, Z. Liu, Y. Sun, C. Chen, H. Peng, M. Schmidt, D. Prabhakaran, B. Bernevig, C. Felser *et al.*, Nat. Commun. **10**, 1 (2019).

[47] V. V. Cheianov, V. Fal'ko, and B. Altshuler, Science **315**, 1252 (2007).

[48] J. Cserti, A. Pályi, and C. Péterfalvi, Phys. Rev. Lett. **99**, 246801 (2007).

[49] C. W. J. Beenakker, Rev. Mod. Phys. **80**, 1337 (2008).

[50] G.-H. Lee, G.-H. Park, and H.-J. Lee, Nat. Phys. **11**, 925 (2015).

[51] W. Chen, L. Jiang, R. Shen, L. Sheng, B. Wang, and D. Xing, Europhys. Lett. **103**, 27006 (2013).

[52] S. Datta, *Electronic Transport in Mesoscopic Systems* (Cambridge University Press, Cambridge, 1997).

[53] C. W. Groth, M. Wimmer, A. R. Akhmerov, and X. Waintal, New J. Phys. **16**, 063065 (2014).